

Hot spot formation in tumor vasculature during tumor growth in an arterio-venous-network environment

M.Welter^a, K.Bartha^b, H.Rieger^{a,*}

^a*Theoretische Physik, Saarland University, PF 151150, 66041 Saarbrücken, Germany*

^b*Department of Medical Biochemistry, Semmelweis University, Budapest, Hungary*

Abstract

Hot spots in tumors are regions of high vascular density in the center of the tumor and their analysis is an important diagnostic tool in cancer treatment. We present a model for vascular remodeling in tumors predicting that the formation of hot spots correlates with local inhomogeneities of the original arterio-venous vasculature of the healthy tissue. Probable locations for hot spots in the late stages of the tumor are locations of increased blood pressure gradients. The developing tumor vasculature is non-hierarchical but still complex displaying algebraically decaying density distributions.

Keywords: Angiogenesis; tumor growth; vascular networks; cancer; blood flow.

*Corresponding author Tel.: +49 681 302 3969; fax: +49 681 302 4899.
E-mail address: h.rieger@mx.uni-saarland.de (H.Rieger)

1 Introduction

Tumors that grow inside vascularized tissues remodel their vascular environment in a characteristic way. Tumor cells secrete growth factors, the most prominent being vascular endothelial growth factor (VEGF) that diffuse into the surrounding tissue. This initiates a vascularization program that is denoted as tumor-induced angiogenesis (Carmeliet and Jain, 2000). The lumen of blood vessels is surrounded by endothelial cells (ECs), which express VEGF receptors that stimulate EC migration and proliferation upon binding to VEGF. Existing blood vessels generate sprouts that migrate through the extracellular matrix, along a chemotactic gradient if present or guided by receptors like those from the Eph family and their ephrin ligands (Kullander and Klein, 2002; Carmeliet and Tessier-Lavigne, 2005) or just randomly in the absence of any guidance clue. As a result new blood vessels are formed in the peritumoral region, where the microvascular density (MVD) is increased. This improves the oxygen and nutrient supply of the periphery and leads to proliferation and expansion of the tumor.

Inside the tumor the formation of new vessels decreases in spite of an abundance of growth factors and the vascularization program is switched from sprouting angiogenesis to circumferential vessel growth. Experiments demonstrate that certain guidance molecules like EphB4 expressed by tumor ECs act as a negative regulator of blood vessel branching and vascular network formation (Erber et al., 2006). In addition to a drastic dilation of the blood vessels in the tumor center a massive vessel regression inside the tumor is observed (Holash et al, 1999; Maisonpierre et al., 1999) leading to a much lower MVD in the tumor center. Regression of blood vessels inside the tumor can be evoked by the presence of angiogenic agonists like angiopoetin (Holash 1999a, 1999b) or by mechanical solid stress in conjunction with a leaky and disorganized vessel structure leading to vessel collapse.

This scenario deviates from the prevailing picture that most tumors and metastases originate as small avascular masses that belatedly induce the development of new blood vessels once they grow to a few millimeters in size (Folkman, 1971; 1990). Instead tumors rapidly coopt existing host vessels to form an initially well-vascularized tumor mass, which in later stages attains its characteristic morphology, which is characterized by (Paku, 1998; Holash 1999a, 1999b; Döme et al., 2002): The tumor is compartmentalized into a perimeter region with MVD much higher than in the normal tissue, a well vascularized tumor periphery, and a tumor center with a very low MVD. In the tumor center necrotic regions are threaded by a few very thick vessels surrounded by 100-200 μm thick cuffs of viable tumor cells. This is expected to be the general course of development of a tumor vessel network that grow in a vascularized tissue.

Recently two of us introduced a mathematical model (Bartha and Rieger, 2006) predicting the dynamics of vascular network formation based on the mechanisms identified experimentally and described in part above. Its basic ingredients are a dynamic network, in which links, representing vessels, can be added or removed or altered (in diameter and other parameters), a cellular automaton representing the growing tumor, and two concentration fields mediating the interaction between the network and the tumor cells. The links of the network, modeled as pipes carrying an ideal pipe flow, constitute the sources of the oxygen or nutrient concentration field, and the tumor cells are sources of the growth factor concentration field. Generation and removal of vessels or tumor cells are stochastic processes with transition probabilities that depend on local concentrations of oxygen and growth factor, blood flow and duration of under-oxygenation. The model displays the characteristic features of tumor vasculature described above and it is robust against parameter variations and various refinements (Welter et al., 2007) as well as the choice of space dimensionality (Lee et al., 2006).

Here, the global characteristics of the emerging morphology of the tumor vasculature, like the radial dependencies of MVD, tumor density, blood flow etc., were independent of the details of the original vasculature. However, local characteristics, like the formation of highly vascularized regions in the tumor center, the so called “hot spots” (Weidner, 1995; Belien et al., 1999), could not be analyzed since the original vessel network was assumed to form a regular lattice and the original blood flow imprinted via boundary conditions was directed along the diagonal of the underlying lattice. As a result, the surviving thick vessels threading the fully developed tumor where also

running along this diagonal and these represented the only hot spot, always occurring in the same location of the tumor network. Since the analysis of hot spots are an important diagnostic tool in cancer treatment (Weidner, 1995; Belien et al., 1999; Pahernik et al., 2001) it is highly desirable to understand the mechanisms determining their development in growing tumors.

The main hypothesis we intend to push forward in this work is that hot spot formation in tumors is connected to local characteristics of the original vascular network. For this reason it appears mandatory to start with a realistic initial vasculature, reflecting the typical arterio-venous organization of the blood vessel network in healthy tissues. The construction of such a network consisting of two interdigitating hierarchical trees, an arterial and a venous tree, under the constraint that the lowest level, the capillaries, provide a homogeneous supply of oxygen in the tissue, is a highly non-trivial task already in a two-dimensional set-up. A mathematical model for the stochastic generation of an arterio-venous network was developed in (Gödde and Kurz, 2001) and a modified version of it is used as the starting configuration of the vessel network in our model. This is based on the ideas developed in our previous work (Welter et al, 2007) for a regular starting network and adapted to the presence of arteries and veins with varying vessel radius and blood flow parameters. The purpose of this work is to describe the transformation of the initial arterio-venous vasculature into a non-hierarchical tumor vasculature with that displays still complex properties characterized by algebraically decaying density distributions. In particular it leads to the formation of hot spots and the most probable location of the regions with highest vascular density can be predicted from an analysis of pressure gradients in the original network.

The paper is organized as follows: In the next section the model is defined, including the method to construct an initial arterio-venous network. Section 3 presents the results for global properties of the tumor vasculature for a choice of parameters that is guided by experimental data for melanoma. These results include a discussion of the emerging morphologies; radial distributions of vessel density, vessel radius, tumor density, flow rates, shear forces etc., vessel statistics, parameter dependencies and drug flow. In section 4 we analyze the spatial inhomogeneities and the hot spot formation of the tumor vasculature. Section 5 concludes the paper with a discussion.

2 Mathematical Model

Our mathematical model contains discrete elements and continuous fields. The tumor is represented by a set of occupied sites on a lattice and the vascular system by a network of connected tubes which occupy lattice bonds. The continuous part involves a O_2 field as nutrient supply and a growth factor (GF) field for angiogenic signaling. The temporal evolution is governed by stochastic processes according to which the automaton state is successively updated. An exhaustive description is given in our previous publication (Welter et al., 2007), but since the introduction of an arterio-venous network and some refinements have lead to a few changes we give a comprehensive overview here.

2.1 Definition of the system state

As illustrated in Fig.1, we study a quasi two-dimensional case, where the arrangement of vessels and tumor cells (TCs) is subject to a regular triangular lattice with lattice-constant δ and size $l \times l = n$. Each lattice site can be occupied each with a single tumor cell. We define T as the set of sites currently occupied by viable TCs. Non-occupied sites represent normal tissue, which we assume to be homogeneous although this is not the case in reality. Likewise lattice bonds can be occupied with vessels. The vasculature is modeled as network of connected ideal tubes. We can formally describe its topology by a graph $G = (N, V)$, where the edges in $V = \{(i, j), i, j \in N\}$ represent vessel segments which we also denote as vessels. The elements in N refer to attached junction nodes. Note that vessels run parallel to the lattice axes and that node locations coincide with lattice sites. We further refer to various properties via sub-scripts, for example the site location of a node i is given by \mathbf{x}_i , while q_a, r_a, l_a denote flow-rate, radius and length of some vessel a .

Blood flow is an important part of our modeling. We assume steady-state laminar flow through the network. Given the pressure gradient $\Delta p = (p_i - p_j)/l$ between the ends of a vessel (i, j) , Hagen-Poiseuille’s Law determines the flow rate $q \propto r^4 \Delta p / \eta$ and wall shear-stress $f_a \propto r \Delta p$. To account for the complex non-Newtonian fluid behavior of blood it is common to introduce an effective viscosity $\eta = \eta_{plasma} \eta_{rel}(H, r)$ depending on local vessel radius r and hematocrit H . We use the empirical formula derived by Pries et al. (1994), where the precise definition can be found. For simplicity we neglect the phase separation effect and set the hematocrit to 0.45, the average in the human body. To find the nodal pressures we solve the system of linear equations which arises from the application of mass-conservation at junctions. Appropriate boundary conditions must be present. Our arterio-venous trees require them only at the ends of the major supply-and drain vessels. We have chosen to set the respective nodal pressures to fixed values $P^{(b)}(r)$ based on the vessel radius.

Vasculature and tumor interact via the growth factor field c_g and the O_2 field c_o . The latter is given by the reaction diffusion equation $\Delta c_o - \kappa c_o + \alpha(c_o^{(B)} - c_o) = 0$, where sources are present at vessel locations and sinks are distributed everywhere. We solve for steady states, because the relaxation time is of the order of seconds while configuration changes at the cellular level take hours. The coefficients have the following meaning: κ is a tissue dependent consumption rate, $c_o^{(B)}$ the blood oxygen level and α the source strength coefficient incorporating local vascular area-fraction and wall permeability. Thereby a number of assumptions were made: (i) O_2 uptake is supply-limited so that a linear approximation to the low- PO_2 regime of a Michaelis-Menten relationship is reasonable. (ii) Blood- PO_2 is constant throughout the vasculature. (iii) Vessels contribute equally to O_2 supply, i.e. α is a constant $\alpha^{(0)} > 0$ at occupied sites, ignoring differences in wall thickness, surface area, etc. Note that the presence of the sink-term κc_o ($\kappa > 0$) would lead to exponentially decaying distributions around point sources. Indeed, experiments show an approximately linear PO_2 decay from the outer vessel wall ranging ca. 150 μm into the tissue.

In analogy, we assume that due to binding and degradation GF has a limited range which is explicitly given by $R^{(g)}$. Let us denote T_{uo} as the set of underoxygenized sites among $\mathbf{x} \in T$. These are characterized by $c_o(\mathbf{x}) < \theta_o^{(prol)}$ where $\theta_o^{(prol)}$ is a threshold parameter. Under the assumption that TCs produce GF at a constant rate the formulation of a diffusion-reaction equation leads to a simple solution via a Greens function approach where c_g is given as $c_g(\mathbf{x}) = \sum_{\mathbf{x}' \in T_{uo}} \tilde{g}(\mathbf{x} - \mathbf{x}')$. For simplicity, convenience and efficiency, we use a linearly decaying “Greens function”: $\tilde{g}(r) \propto \max[0, 1 - r/R^{(g)}]$.

2.2 Definition of the dynamical processes

Tumor and vascular network dynamics are governed by the stochastic processes described below. In practice, when we analyze the model by Monte-Carlo simulations, we iteratively update the system by a fixed time step $\Delta t = 1h$. Per step, a sweep is done for each process. After that the configuration has changed and therefore O_2 and GF fields are recomputed. This is reasonable if δ is sufficiently smaller than the rates at which changes are introduced.

TC Proliferation: New TCs occupy empty neighbor sites $\mathbf{x} \notin T$ with probability $\Delta t / t_{TC}^{(prol)}$ if the local oxygen level is high enough $c_o(\mathbf{x}) > \theta_o^{(prol)}$. This resembles the behavior of real tumors (Bru et al., 2003; Drasdo and Höhme, 2005) where proliferation is restricted to a small band behind the invasive edge due to space and nutrient constraints. (*Fig.2a*)

TC Death: TCs are removed with probability $p_{TC}^{(Death)} = 1/2$ if the local O_2 level is less than $\theta_o^{(death)}$ for longer than $t_{TC}^{(uo)}$. Since TCs adapt to low oxygen conditions (Iyer et al., 1998), $\theta_o^{(death)} = \theta_o^{(prol)}/10$ is very small. For simplicity the survival time $t_{TC}^{(uo)}$ has been given a fixed value, in spite of strong variations among genotypes (Yu et al., 2002). (*Fig.2b*)

Angiogenesis: The presence of GF stimulates angiogenic sprouting at a vessel occupied site \mathbf{x} in the following way. First it is required that the local GF concentration $c_g(\mathbf{x})$ is larger

than the threshold $\theta_g^{(prot)}$. Evidently no sprouting happens inside the tumor (Holash et al., 1999). Indeed molecular pathways (via EphB4 and its ligand ephrinB2, expressed in tumor endothelial cells) have been identified recently which are related to the switch from sprouting to circumferential growth (Erber et al., 2006). Therefore it is also required that parent vessels have not been inside the tumor for longer than $t_{EC}^{(switch)}$. We characterize a position as “inside” if radial distance to the tumor center is smaller than the extent of the tumor in the respective direction. A vessel is inside the tumor if the midpoints of at least 50% of all occupied bond are inside. Our vessels carry a type information: they are either artery, vein or capillary. Vessels created via sprouting as described here are always of capillary type, while the type of the initial vessels is given by construction of the arterio-venous trees. For our base case, we require the parent vessel to be either of venous or capillary type, automatically including active (capillary-)sprouts. These sprouts can thus already branch out into sub-sprouts. We exclude arteries because the thicker endothelium and presence of smooth-muscle cells makes sprouting less likely. The last requirement is that adjacent bifurcations must be at least $l^{(spr)}$ μm away since endothelial cells close to bifurcations also do not form sprouts. If those criteria are fulfilled an initial segment of length δ and radius $r^{(init)}$ is appended with probability $\Delta t/t_{EC}^{(sprout)}$, possibly splitting the parent vessel. At successive iterations more such segments are added to the tip with probability $\Delta t/t_{EC}^{(sprout)}$. On contact, it connects to other vessels forming a potentially blood perfused loop. Thereby the initial sprout direction is given by the steepest GF descent (Gerhardt et al., 2003). Furthermore, sprouts cannot extend indefinitely (Nehls et al., 1998). Therefore a “countdown” of $s^{(max)}$ hours terminates the sprouting behavior upon expiration (see below). The respective internal timer variable is inherited from the previous sprouting tip. Note that tumors grow by co-opting vessels but no explicit modeling is required for this since TCs proliferate in a separate layer without mechanical interaction. (*Fig. 2c,d*)

Vessel Collapse: Vessel in normal arterio-venous networks have differing amounts of support structures around the endothelium: the basement membrane, pericytes and smooth-muscle cells. In tumors interaction/adhesion between these components is often disrupted (McDonald and Choyke, 2003). There one finds vessels with fragmented and multi-layered basement membranes and detached pericytes. Further the lumen of such vessels is often completely collapsed and/or the endothelium is also found in a state of regression. Therefore, we believe that it is physiologically sound that the survival time of initially healthy vessels depends on how well the vessel wall is developed, i.e. capillaries with just the membrane around the endothelium should collapse earlier than thicker arterioles. We realize this by a “degree-of-maturation” variable w which is initialized with data for the wall thickness in normal vessels (Pries et al., 2005), depending on vessel radius r . Using a rough approximation, we set $w = 2r(0.65 - 0.2 \log(2r))$. Inside the tumor, vessels are continuously degraded at the rate Δw . While w is larger than the threshold $w^{(c)}$, a vessel does not regress, meaning the segment is not removed from the network. Furthermore, physiological wall shear stress levels can dose dependently inhibit endothelial cell apoptosis, while long term reduction can cause vessel regression (Dimmeler and Zeiher, 2000). We include this by constraining removals to vessels with shear forces f less than the threshold $f^{(c)}$. In tumors, impaired blood flow and thereby low shear stresses might be the result of increased solid pressure compressing the vessels. Also our previous work has shown that shear force correlated collapses lead to realistic network morphologies. If collapse inhibiting effects do not apply, segments are removed with probability $p^{(c)}$. For a dose dependent effect we set $p^{(c)} = p_{full}^{(c)} = p^{(c,max)}(1 - f/f^{(c)})$, with the constant parameter $p^{(c,max)}$. Note that sprouts are completely excluded from the above processes. In section 3.3 we also discuss the effect of restricting collapses to a thin band behind the invasive edge, using the collapse probability $p_{ring}^{(c)}$ as defined there. (*Fig. 2e*)

Vessel Dilation: Exposure to growth factors is also associated with unphysiological vessel dilation, in particular in tumors which is related to the mentioned switching to circumferential growth inside the tumor (Erber et al., 2006). Experiments (Döme et al., 2002) indicate that

vessel diameters increase continually to an upper limit. In the model the dilation process works as follows: Each bond occupied by a non sprouting vessel a increases the radius r_a by Δr_a with probability $\Delta t/t_{EC}^{(dil)}$ if $r_a < r^{(max)}$, if the center of the bond is inside the tumor and if the local GF concentration is larger than $\theta_o^{(prol)}$. The increment $\Delta r_a = \delta^2/2\pi l_a$ corresponds to the surface area of an additional EC contributed to the total surface area of the segment. To account for surface tension, a smoothing effect is generated by dilating the thinnest vessel at junction bonds. (*Fig.2f*)

2.3 Arterio-venous tree generation

Vasculature in living tissue exhibits a tree like structure. Few thick arteries branch out into arteriolar microvessels. Terminal branches are connected to the capillary bed, a dense network consisting of thin vessels where most of the exchange with the surrounding tissue happens. Further upstream blood is collected in venoules which fuse into thick veins. In the sense of some optimality measure, the design goal of such structure is to provide sufficient amount of nutrients to tissue ,while minimizing the effort to keep the circulatory system operating.

Numerous ways to generate vasculature in silico have been proposed in the literature for example fractal approaches based on L-Systems (Mandelbrot, 1991) or optimization based geometrical construction (Schreiner and Buxbaum, 1993). Most of which concentrate on building the supplying arteries only, neglecting explicit modeling of capillaries and veins. A deterministic manual construction of a single configuration would have been unsuitable and difficult with respect to the desire to obtain the flexibility to create a wide range of configurations while retaining physiological properties.

Gödde and Kurz, (2001) presented a method to grow and remodel vascular trees stochastically according to probability functions that depend on local system properties. The simultaneous construction of arterial and venous trees makes their approach well suited for generating an initial vasculature for our tumor simulator, where a complete network including draining venoules is required.

The general idea is to grow purely random arterial- and venous trees on a lattice, under exclusion of already occupied sites. Followed by iterative shear-stress guided further growth and regression at the tree leafs, whereby a well perfused space filling network evolves.

2.3.1 Network construction

The mathematical model for the vasculature is identical to the definition in the tumor simulation: the network is identified with a graph plus additional geometric and hemodynamic properties, embedded in a triangular lattice.

Our initial condition for the growth stage consists of several prescribed segment chains for arteries and veins which become the major vessels in the upper tree levels. Their length and position is drawn from a uniform distribution within reasonable bounds.

The basic structural element for further growth is a tripod consisting of three vessel segments arranged in 120° angles. These tripods are appended successively at randomly chosen tree leafs. Exceptions are the initial chains where all included sites are candidates for adding elements. Thereby overlap with already occupied sites/bonds is forbidden, and so the process continues until there are no more valid configurations where tripods could be added. The resulting network consists of at least two binary trees with at least one arterial and one venous side.

To compute blood flow vessel radii must be known. ‘Murray’s Law’ (Murray, 1926) relates the radius of a parent vessel a to the radi of branches b,c . $a_r^\alpha = b_r^\alpha + c_r^\alpha$, where $\alpha = 2.7$ is a realistic value as used by Gödde and Kurz. The radii of the tree leafs are preset to $4 \mu\text{m}$ for arteries, and $5 \mu\text{m}$ for veins. Thus all other radii can be computed in a recursive algorithm which visits a vessels once its descendants have been processed.

To get a complete network, capillary segments have to be added. We simply loop through the bonds on the lattice and add a connection a with $a_r = 3.5 \mu\text{m}$ if it connects an arterial tree with a venous tree. As additional constraint a connection is not added if more than three vessels would

meet at a site. Capillaries are not constraint to connect leaf nodes exclusively, however all vessels at the respective node pair must fulfill $r < r^{(cap)}$.

The second stage of construction consists of iterating: radii determination, capillary creation, flow rate and shear force computation, capillary removal, and remodeling sweep, until the system reaches a steady state. Our remodeling procedure works as follows: One of *growth*, *death*, *idle* is drawn for each segment according to the respective probabilities $p_g, p_d, 1 - p_g - p_d$, where $p_g + p_d \leq 1$. Relating these to shear stress f such that $p_g \nearrow f$ and $p_d \searrow f$ leads to expansion in well perfused branches while non-perfused branches regress and make room for growth of interdigitating patterns. The probability relationship we used here is as follows:

$$\begin{aligned} \tilde{f} &\leftarrow \frac{\ln f - \min_a \{\ln f_a\}}{\max_a \{\ln f_a\} - \min_a \{\ln f_a\}} \\ \tilde{r} &\leftarrow 1 - \min \left\{ 1, \frac{r - 4\mu m}{10 - 4\mu m} \right\} \\ \tilde{p}_g &\leftarrow (\tilde{f} + p_0) \cdot \tilde{r} \\ \tilde{p}_d &\leftarrow (1 - \tilde{f} + p_0) \cdot \tilde{r} \\ p_g &\leftarrow \tilde{p}_g / (\tilde{p}_g + \tilde{p}_d) \\ p_d &\leftarrow \tilde{p}_d / (\tilde{p}_d + \tilde{p}_d) \end{aligned}$$

To prevent unnatural situations where thick vessels have too many capillary branches while still obtaining homogeneous MVD there is the radius term \tilde{r} which decays from 1 at $r = 4$ to 0 at $10 \mu m$. The offset p_0 is added for two reasons: to lower the rate at which un-circulated initial vessels regress, and to add fluctuations to reduce deadlocks in high shear stress regions. Leaf segments labeled as dying are removed. The removal is constraint to leafs in order to maintain the binary tree structure. Next, new elements are added to growing segments, whereby one of all admissible configurations is randomly picked. Beside tripods we also allow single segments to be added in order to allow vascularization of regions where bottlenecks in between major vessels would block access.

2.3.2 Construction results

In order to study typical tumor-network morphologies we must simulate a sufficiently large domain: 12×10 mm. To obtain a specific MVD we adjust the tree generators bond-length $\delta^{(gen)}$ and set the lattice size accordingly. Due to the two-dimensionality of our system we measure MVD as the fraction of occupied sites. Furthermore we chose $\delta^{(gen)}$ to be a multiple of the tumor lattice bond-length δ so that the network can be taken to the tumor model by superimposing the lattices. Based on the average for human skin, 100 vessels per mm^2 cross-section (Döme et al., 2002) which implies $10 \mu m$ inter-vessel spacing, we set $\delta^{(gen)} = 60 \mu m$ and $l = 200$.

Due to the hierarchical design of real vasculature, blood-pressure correlates well with vessel radius. Plotted, it exhibits a sigmoidal shape (Pries et al., 1995). In order to prevent physiologically inconsistent pressure gradients across our networks, we adapt the boundary pressure by an approximate formula. ($p(r) = 0.133(18 + 72/(1 + \exp((r + 21\mu m)/16\mu m)))$ kPa; r is negated if it is the radius of an arterial segment).

As illustrated in Fig.3, we have chosen four basic layouts. The inlet schematics indicate bounds for the positions and lengths of the initial chains. These are drawn from uniform distributions within a prescribed range, whereas their types (arterial or venous) are unalterable. The initial conditions were deliberately chosen, motivated by the observation that vasculatures exhibit relatively thick straight vessels down to a certain level in the hierarchy as can be seen in photos from the CAM (Mironov et al., 1998), or in recent 3d vascular imaging experiments (Cassot et al., 2006).

Quantitatively we have compared our data with scatter plots of hemodynamic properties shown in (Gödde and Kurz, 2001). They are near identical to the original and therefore not shown directly. Instead we refer to Fig.10 where tumor vessels are also included.

2.4 Parameters

In what follows we analyze the model with parameters guided by experimental data (Döme et al., 2002) for human malignant melanomas.

The lattice bond length δ is set to 10 μm , the typical diameter of TCs and ECs. The initial tumor is an eden-grown cluster of 1000 cells and 300 μm in diameter. The initial vasculature has been discussed. Growth and death rate parameters as well as oxygen and growth factor diffusion parameters have been discussed in detail in (Welter et al., 2007).

To recapitulate, we set the TC proliferation time $t_{TC}^{(prol)}$ to 10 h, sprout initiation/extension time $t_{EC}^{(sprout)}$ to 5 h, the time until regression of loose sprouts $s^{(max)}$ to 100 h (Nehls et al. 1998), the minimum distance between bifurcations $l^{(spr)}$ to 20 μm , the initial sprout radius $r^{(init)}$ to 4 μm , the time until sprouting switches to circumferential growth $t_{EC}^{(switch)}$ to 24 h, EC proliferation time for circumferential growth $t_{EC}^{(dil)}$ to 40 h and the maximum radius $r^{(max)}$ to 25 μm . For the continuous fields we set the O_2 source coefficient $\alpha^{(0)}$ to 0.002, the consumption coefficient κ to $\kappa^{(Nmm)} = (90 \mu\text{m})^{-2}$ in normal tissue and to $\kappa^{(T)} = 4\kappa^{(Nmm)}$ in tumor tissue to get halve the diffusion distance. Here the blood oxygen level $c_o^{(B)}$ can be chosen arbitrarily because it appears as global scaling factor in the solution. The model however can be adjusted accordingly by scaling the threshold parameters. Therefore we set it as previously to the hematocrit value $c_o^{(B)} = 0.45$ (which is constant here). We set the threshold for TC proliferation $\theta_o^{(prol)}$ to $0.3 \approx 0.9\langle c_o \rangle$ and threshold for extreme under-oxygenation $\theta_o^{(death)}$ much smaller to $\theta_o^{(prol)}/10$. The TC survival time under hypoxia $t_{TC}^{(uo)}$ is set to 100 h. The growth factor radius $R^{(g)}$ is set to 200 μm , and the vessel proliferation threshold $\theta_g^{(prol)}$ is set very low to 10^{-4} so that all vessels within the full GF radius are affected. Parameters related to vessel regression are as follows. The critical shear force $f^{(c,max)}$ is set to 1 Pa. Note that average shear stress is $\langle f \rangle \approx 10$ Pa. The collapse probability $p^{(c,max)}$ is set relatively high to 0.1. The dematuration rate Δw is set to 0.04 $\mu\text{m}/\text{h}$, resulting in regression delays from 93h (4 μm vessels) to 625h (50 μm vessels).

3 Results

We run 10 Monte-Carla simulations for each of the four initial vascular setups as explained above and shown in Fig.3. We generated different initial networks for each run by changing the random number seed for the construction algorithm. The vessel density distribution in the vascularized regions is generally very homogeneous by design since we attempt to maximize the lattice occupation. Normally the networks fill less than the entire rectangular domains. We accept this if the support area is sufficient for tumor growth till the end at $t = 1200\text{h}$

Fig.4 shows the evolution of the model using vasculature configuration (a). Not shown is the very first stage of tumor growth which includes the following. High tumor O_2 consumption leads to decreased O_2 levels inside the nucleus and consequently enables vascular remodeling via growth factor production. Angiogenic sprouting increases the MVD around the tumor, while after a few hours of prolonged exposure to GFs, central capillaries show noticeable increased diameters. The first image shows the tumor at $t = 200\text{h}$ where a dense capillary plexus has been created by angiogenic sprouting around the tumor nucleus. Vessel collapses are not yet occurring there. By $t = 100\text{h}$ the wall maturation w decreased sufficiently though to allow first collapses of the thinnest capillaries with inadequate shear force. We observe this in other simulation runs. The process of angiogenesis and collapse proceeds as the tumor expands. At $t = 400\text{h}$ first regions are visible where TCs have died due to hypoxia. Thick arterioles and venoules don't yet collapse due to $w > w^{(c)}$, though they may have low shear force levels. Fig.5 shows the final tumor at $t = 1200\text{h}$ and Fig.6 shows tumors of the other network configurations. Fig.7 shows a magnified view on the boundary region of the tumor in Fig.5. The tumor masses expand approximately disc shaped. Because of the simple oxygen distribution model where all vessels release O_2 homogeneously, this fulfills our expectations. Normally nutrient exchange happens at the thinnest capillaries. Venoules and arterioles would naturally not contribute to tissue supply as much. This however is not practical

in a two dimensional model because non-oxygen-releasing vessels would be impassable barriers to the tumor. Therefore we require that O_2 content, and wall-permeability is equal for all vessel. The resulting network morphologies show the typical high MVD periphery/peritumoral region and low density center. A general feature of our model seems to be the formation of arterio-venous shunts cause by dilation of vascular pathways that connect to initially available arterioles/venoules. Those paths can consist of neo-vasculature as well as initial capillaries and other vessels. As we expect, most vessels form isolated straight threads, however regions where vessels are densely clustered are also observable.

3.1 Radial distributions

For comparison Fig.9 shows quantities averaged within concentric shells emanating from the tumor center. MVD and TC density are computed as the fraction of occupied sites within a shell. Hemodynamic properties are averaged over occupied bonds only. Mean values of the microvascular density MVD and vessel radius r , reminiscent of results from earlier work, agree well with experiments (Döme et al., 2002) as we have discussed for similar data in (Bartha and Rieger, 2006). Döme et al. measured the MVD and MVR in three distinct regions: the central region, a $100\mu m$ wide peripheral band just behind the invasive edge, a $200\mu m$ wide peritumoral region outside the invasive edge. In the central region, they found 25% MVD of normal tissue, and up to 200% in the peritumoral region. The vessel perimeter grows linearly from $50\mu m$ and assumes a plateau at $200\mu m$ by day 15.

In contrast to results for a regular vascular network (Bartha and Rieger, 2006; Welter et al., 2007), flow rates and shear force now show a plateau like the vessel radius which is expected since the flow boundary condition on the regular network lead to unrealistic star shaped morphologies, directing all blood flow through the center. The hierarchical networks here do not introduce such obvious problems. Not shown is data for the blood-pressure gradient dp/dl which decreases monotonically toward the center by more than one order of magnitude. The blood flow rate q is proportional to $r^4 dp/dl$ and increases on average toward the center beyond a small local minimum at the invasive edge. Thus the r^4 dependency of the radius outweighs the pressure drop. The shear force dependency is $r dp/dl$, leading to a decrease respectively.

3.2 Vessel Statistics

Fig.10 shows scatter plots of hemodynamic variables against the vessel radius r . While providing more information about their distribution over vessels, such plots are also common in the literature. Compared to (Gödde and Kurz, 2001) we get a good match. The data is from a single simulation run. Data from the initial vasculature and from the tumor vasculature at $t = 1000h$ are both displayed in the same plots.

For the initial network we generally observe that the variance of the flow related parameters increases drastically towards the capillaries. While this might be an artifact of the artificially constructed network, averaged values show physiologically sound characteristics.

The dilation of tumor internal vessels leads to samples clustered at the maximum dilation radius ($r^{(max)} = 25\mu m$) and therefore one observes larger ranges of hemodynamic variables. In particular, the blood pressure in tumor vessels ranges from typical arterial values to venous values as these vessels connect both sides via shunts by a continuously varying pressure potential. Consequently the pressure in arteries, over which the tumor as grown, is lower than normal while the pressure in former veins is elevated.

In the flow computations we fix the pressure difference between supply-and drain, which means that the flow rates in the major vessels are determined by the total resistance of the network. Lowering this resistance by arterio-venous shunts increases the blood throughput, which is evident in Fig.10c when observing the increased flow rates in the thickest vessels. This increase is in particular pronounced on the venous side. The flow rate in the initial network grow slightly stronger with the radius on the arterial side than on the venous. Therefore the difference between

tumor network and normal network is less pronounced for arteries. Interestingly many of the dilated capillaries at $r^{(max)}$ fall below the normal average flow rate.

In contrast, most non-dilated small capillaries which are obviously located in the outer rim fall in the same ranges than normal vessels. A few vessels though show significantly lowered flow and velocity values. In section 3.4 we study the impact of them upon drug delivery.

3.3 Parameter dependencies

Here we discuss the role of the most sensitive parameter dependencies and model changes. The large shear force variations among capillaries in the original vasculature leads us to the question whether an absolute threshold for the collapse criterion is appropriate. Therefore we also checked the result of setting $p^{(c)} \propto 1.0 - (f/f_{init})/f^{(c)}$ for $f/f_{init} < f^{(c)}$, where f_{init} is the shear force in the of the original vasculature. The result is less MVD fluctuations in the samples and also locally a more homogeneous distribution.

In the present model variant, vessels can collapse any time after degradation ($w < w^{(c)}$), depending on shear-stress. It is however also an option to restrict vessel collapses close to the tumor boundary. For example, it has been suggested that the death of tumor cells releases solid pressure from nearby vessels which is otherwise exerted by the tumor (Griffon-Etienne et al., 1999). In previous papers we assumed the existence of a stable radius, preventing collapses in the center where vessel radi are larger. Indeed, the EphB4 signaling mechanism which is related to circumferential growth, can also lead to reduced leakiness, tightened EC junctions and increased endothelium/pericyte interaction (Erber et al., 2006), making an actual stability improvement plausible. Again, we have implemented this very simplistically by modulating the collapse probability: $p^{(c)} = p_{ring}^{(c)} = p_{full}^{(c)} \cdot \Theta(x - x_T - \delta^{(c)})$, where Θ is the Heaviside function, x_T the radial tumor extend, and $\delta^{(c)}$ is the ring width measured from the invasive edge. The result obviously depends strongly on the time vessels spend in the collapse region, given implicitly by $\delta^{(c)}$, Δw , the radius r and the tumor expansion rate. If this time is of the order of the mean survival time $\Delta t/p^{(c)}$ a transition occurs toward a highly vascularized center, reminiscent of the ‘‘percolation transition’’ analyzed previously (Bartha and Rieger, 2006; Welter et al. 2007; Lee et al., 2007). In this case the random collapse-process also plays a more dominant role because many weakly-perfused vessels can survive whereas, using $p_{full}^{(c)}$, these vessels would eventually regress if one just waits sufficiently long. Fig.11 shows respective simulation results, using $\delta^{(c)} = 400\mu\text{m}$, $f^{(c,max)} = 3\text{Pa}$ and all other parameters unchanged. One can see increased formation of high-MVD hot spots and less isolated threads than for example in Fig.5. The MVD is slightly higher, but easily tunable by $p^{(c,max)}$ and $f^{(c,max)}$. Generally, $p_{ring}^{(c)}$ also leads to less fluctuations with respect to initial networks apparently because initially thick vessels provide a backbone which never collapses due to $w > w^{(c)}$ while being in the ‘‘collapse ring’’.

By default sprouting is allowed from veins and capillaries but not from arteries. Enabling sprouting from all vessels naturally leads to ca. 40 % higher MVD in the boundary, while the central MVD also depends on the collapse model. Using parameters with $p_{ring}^{(c)}$ so that the effect of $p_{ring}^{(c)}$ becomes significant, i.e. near a transition to fully vascularized tumor, the MVD will increase, but otherwise not. Because the boundary becomes more homogeneously vascularized also the O_2 field becomes more homogeneous. But with the current O_2 proliferation threshold $\theta_o^{(prol)} \approx 0.9\langle c_o \rangle$ this does not alter the tumors expansion rate due to TCs proliferating around smaller low- O_2 regions and enclosing them. We expect this to be different in reality. TCs would likely migrate into low- O_2 regions driven by the pressure of the surrounding tissue where they remain in a quiescent state.

3.4 Drug flow

In order to assess the effects of typical tumor network morphology on transport of drugs into and through the tumor, we analyze the time-dependent concentration distribution of drug during a

continuous injection into the blood stream, starting at arterial boundary nodes.

The computational model for drug flow in a vascular network is described in detail in (Welter et al., 2007; McDougall et al., 2002). The starting point is a given configuration for the vasculature in our model with precomputed/prescribed variables for flow, flow velocity, segment length, and radius of the pipes in the network. In addition, a mass parameter m is now associated with segments describing the amount of drug in the segments volume. The mass content m is deterministically updated in successive time steps as follows: First the drug amount flowing out of segments is determined and added to respective node-mass variables. Under the assumption of perfect mixing, the nodal masses are then redistributed into further downstream segments. Thereby mass conservation is strictly enforced. A detailed description can be found in (Welter et al., 2007). The most severe limitation of this model is that there is no exchange with extra vascular space and therefore also no uptake by the tumor.

The results in the following were obtained with an continuous injection into the vasculatures from the case $f^{(c,max)} = 1$. From $t=0$ on, blood with solute drug at conc. $C^{(init)} = 1$ flows into the vasculature which is initially filled with “clean” blood. We don’t consider bolus injections because the flow rates are of the order of mm/s, which is sufficient to saturate 80-100% of the vessels within seconds, depending on the network configuration.

Fig.15 shows a sequence of snapshots from configuration (a) $t=0$.. 6.6s. Drug enters the system via the arteries and flows downstream with a sharp transition at the drug/clean interface. When vessels merge in upstream direction mixing with clean blood occurs and so the concentration increases moderately in the veins. After 20 s near full saturation is achieved. Dilation of tumor internal vessels and apparent direct connections to feeding arterioles lead to comparably fast filling with drug, whereas a few regions in the highly vascularized boundary take significantly longer to be filled. Depending on the exact network configuration we have consistently encountered such strong variations in drug delivery to the outer rim. It is likely to be caused by the shunts which lead to decreased flow rates in the surrounding tissue. Fig.10c also shows the existence of capillary sized tumor vessels with very low flow rates of the order of $10^3 \mu\text{m}^3/\text{s}$, corresponding to an average flow velocity of the order of $10 \mu\text{m}/\text{s}$. The average flow velocity over all vessels in the original network is $\sim 1.8 \text{mm}/\text{s}$.

Quantitative analysis of drug efficiency impact is only possible to a limited degree due to the lack of tumor uptake modeling and because even few surviving TCs can grow a new tumor mass. None the less we measured statistics for the total amount of drug in the vasculature. Fig.16a for example, shows the fractional length of the tumor vessel-network for which the maximum drug-concentration was larger than indicated on the “ c ”-axis. After 20 s, on average $94 \pm 3\%$ of the vasculature had been exposed to a drug concentration of at least 80%. For higher concentrations the curve decreases drastically. It also shows evidently by the drop at $c=0$ that $4 \pm 3\%$ had not been drug perfused at all. In absolute numbers the latter corresponds to $15 \pm 12 \text{mm}$. Fig.16b shows the fractional length of the tumor vessel -network for which the concentration was larger than the threshold $c = 0.25$ for a total duration greater than indicated on the x-axis as t_e . This measurement was also done at $t=20\text{s}$, thus the exposure time cannot be longer than that. One can see, for example, that $93 \pm 4\%$ of the vasculature had been exposed 50% drug concentration longer than 10s. Considering the flow rates/velocities mentioned above one can expect the remaining few millimeters to be drug perfused within a time frame of minutes. We therefore still believe that the geometry and hydrodynamic flow characteristics do not pose an inherent problem to drug delivery.

4 Hot-spots and spatial inhomogeneities

Already by visual inspection one observes a coincidence of the location of hot spots in the tumor vasculature with the location of the thicker vessels. For example in configuration (a) where an artery is close to a vein, or vice versa, an increased number of vessels survive in between. On the other configuration similar behavior can be observed on smaller scale. The blood pressure in thick vessels is approximately constant compared to the steep drops in the capillary bed. This is due to the orders of magnitudes larger flow conductivity. It is plausible that in (a) for example, a

high global vertical pressure drop leads to high shear forces in between the two major vessels and therefore increased survivability. Furthermore the asymmetry in the shear stress distribution over the vascular trees (meaning that given vessels of a certain radius, the shear stress in arteries is usually higher than in veins; see Fig.10), apparently leads to hot spot formation preferably close to the arterial branches.

This motivates a quantitative analysis of the relation between inter-vascular “blood-pressure” gradients in the original vasculature and the local MVD of the tumor vasculature. This is done as follows: Since new vessels formed during the process of sprouting angiogenesis will experience a shear force proportional to the pressure drop from one end to the other. Therefore we first compute a pressure field $P(\mathbf{x})$ as solution to the Laplace equation $\Delta P = 0$ subject to the boundary condition that P is set to the blood pressure at vessel sites. The resulting field interpolates pressures between adjacent vessels, and would change perfectly linear between two infinite parallel vessels. At any given point, we can obtain the magnitude of the gradient, which we use to compute a spatial average of $\|\nabla P\|$. We do this for $t=0$ h. The resulting mean value $\langle\|\nabla P\|\rangle$, is plotted together with an estimate for the tumor MVD at $t=1200$ h (defined as the fraction of occupied sites) as displayed in Fig.12. The main plot shows the MVD versus $\langle\|\nabla P\|\rangle$ over entire tumors with one data point per simulation run. The correlation coefficient is usually very large ≈ 0.9 for this global measurement. Analogously we analyzed single tumor instances where the averaged is taken locally over randomly distributed small regions (discs with $150\mu\text{m}$ radius). The inset shows the resulting distribution of one such measurement. The correlation coefficient in this instance is already low (≈ 0.4). On average we observed it to vary with the model details and even with the initial vasculature between 0.2 and 0.4.

Fig.13 is a visualization of the statistical correlation observed in the above analysis. We take the data from the system configuration in the simulation run shown in Fig.5. The bottom image (c) shows the site occupation by the vessel network. It is easy to identify the tumor network by its typical structure. In (a), where $\|\nabla P\|$ is displayed, one observes that indeed the local gradients are stronger in the area close to the major artery in the top half, than close to the vein in the lower half. The snapshots on the right column (b) and (d) show respective mean value samples of the left hand side. These distributions show the behavior that zones with elevated $\langle\|\nabla P\|\rangle$ are also probable locations of high MVD.

A plausible argument for the existence of the correlation between hydrodynamic characteristics of the initial network and local morphological features in the evolved tumor vasculature is the following: In regions with originally strong inter-vascular pressure drops, tumor vessels would be less prone to collapse because sprouting forms new connections whose shear-stress is proportional to $\|\nabla P\|$. Thus, shear-stress stabilization would prevent regression in high- $\|\nabla P\|$ regions. Since single collapse events lead to long-ranged collapses of adjacent network sections, we believe that therefore local measurements hardly show correlations. Note that the intra-vascular blood-pressure at in-and outflow vessels is prescribed and depends on the vessel radius. Therefore only the positioning of initial vessels leads to the variety of emerging tumor morphologies.

We further quantify the spatial inhomogeneities by probability distributions for local MVD (Fig.14a), necrotic region size (b) and hot spot size (c). The distributions are estimated via histograms of the respective local measures, whereby we insert data from multiple (40) runs into the same histogram in order to get a smooth curve with reasonably small bin. The MVD in Fig.14a is estimated as fraction of occupied sites within boxes ($250\mu\text{m}$ in size) of a regular grid. The plot displays two peaks. One large at low MVD ≈ 0.07 which decays algebraically with exponent ~ 1.4 till smaller peak at MVD ≈ 0.45 . The latter stems from the high-MVD zone in the tumor periphery. Not included is a peak which appears at MVD=0 due to large non-vascularized regions. The necrotic-region size distribution in Fig.14b plots the probability to find a connected cluster of dead TCs with a certain volume, i.e. number of cells. The hot-spot size distribution in Fig.14c plots the probability to find a connected cluster of a certain number of sites where the local MVD is larger than a threshold value (here 0.15). Therefore we compute an estimate for the MVD for each lattice site as the fraction of occupied sites within a $250\mu\text{m}$ diameter disc. Both of the latter distributions exhibit purely algebraic decay also with the exponent ~ 1.4 .

The fractal dimension d_f is often used to quantify tumor networks and has been found capable

to distinguish them from normal vascular networks (Baish and Jain, 2000). Therefore we do box counting analysis, which is usual practice to estimate d_f for natural objects. Perfect fractals show a power law $N \propto \epsilon^{-d_f}$ in the number of touched boxes N vs. size ϵ , yielding a constant slope in a log-log plot. We typically observe a parabolic shape of the local slope curve with a small constant plateau over half a decade. Due to the problems associated with d_f estimates, such plateaus are often considered sufficient to extract d_f ; see the discussion in (Chung and Chung, 2001). In this context one also speaks of box counting dimension. On average we obtain $d_f = 1.76 \pm 0.03$ for the final internal tumor network; $d_f = 1.79 \pm 0.03$ including high-MVD peripheral region. The error is given by the root mean square deviations among 40 simulation runs with the same parameter set. Fluctuations of this magnitude are very significant, which is why we consider these results as unreliable and also show no data here. Furthermore resembling previous results, we still find our d_f estimate being primarily determined by the MVD.

5 Discussion

The conclusions that can be drawn from the theoretical model for vascular remodeling of an arterio-venous network during tumor growth are manifold: As has already been conjectured on the basis of an analogous model with a regular or lattice-like blood vessel network (Welter et al., 2006) the global characteristics of the emerging tumor vasculature is expected to be independent of the specific details of the initial vasculature: the resulting morphology is compartmentalized into a highly vascularized tumor perimeter, a tumor periphery with large vessels density and dilated vessels and a central region containing necrotic regions with a low micro-vascular density threaded by extremely dilated vessels. The basic mechanisms leading to this morphology are identified as sprouting angiogenesis in the tumor perimeter, a switch of the vascularization program to circumferential growth plus vessel regression within the tumor.

On top of these global feature our model predicts spatial inhomogeneities, visible in drastic MVD variations. These are strongly correlated with the local characteristics of the initial arterio-venous vessel network, which are absent in a regular homogeneous initial vasculature. In simulation runs with identical parameters but different arterio-venous network configuration, cases can be observed ranging from tumors threaded mostly by individual vessels, to tumors that exhibit many dense clusters connected by few short chains. The reason for this variability the asymmetry of the shear force distribution between the arterial and venous side of the vascular trees.

Depending on the details of the initial network in our model the tumor vasculature develops isolated highly vascularized clusters connected by thick vessels. These “hot spots” are also observed in real tumor and serve as an important diagnostic tool in cancer therapy. Already by a visual comparison of the starting network with the final tumor network one observes that hot spots form more frequently in those regions where the starting network contained predominantly arteries. We therefore analyzed the correlation between various local hydrodynamic quantities of the original network (blood pressure, blood pressure gradient, blood flow) and the local MVD in the tumor network and found a significant correlation between local blood pressure gradient of the original arterio-venous network and the most probable locations of hot spots in the tumor vasculature. This is plausible since a high pressure gradient within the vessels implies a high shear force exerted by the blood on the vessel walls, which stabilizes the vessel against collapse and therefore leads to an increased vessel survival probability when the tumor has grown over this region. Since we expect these mechanisms also to be at work in real tumors it should therefore in principle be possible to predict on the basis of an analysis of the blood vessel network in the healthy tissue, where most likely the tumor vasculature develops its hot spots. We note that in our model this hydrodynamic mechanism plays a dominant role in the hot spot formation, whereas potential local variations in pro- and anti-angiogenic effectors within the tumor were not involved but could also play a role in this process.

Remarkably an association between the MVD of the original vasculature in normal tissue and hot spot vascular density in the tumor has been reported for carcinoma (Höckel et al., 2001). Here the MVD of normal tissue was measured far away from the tumor and it was found that it

correlates well with the MVD of the hot spots in the tumor. Our interpretation of this result is that sprouting angiogenesis is not strong in these tumor samples (in fact the MVD in the tumor periphery was increased by only ca. 20%) and hot spots in the tumor represent regions of the original vasculature that could survive vessel collapse due to locally increased pressure gradients. For a reliable check of our hypothesis one would have to analyze the pressure gradients in the vasculature of the normal tissue *before* the tumor grows over it, i.e. under experimental conditions of an implanted tumor for instance.

Various probability distributions that quantify the spatial inhomogeneities of the tumor network in our model turn out to display an interesting behavior, too: The probability distribution of local MVD values as well as the probability distribution of the hot spot volume (defined as the size of connected clusters of regions with MVD larger than the original MVD) have an algebraic tail with exponent ~ 1.4 . Also the size distribution of the connected clusters of necrotic tumor regions showed an algebraic tail (again with exponent ~ 1.4). These power laws indicate a critical state in accordance with the fractal properties of the tumor network: It implies the absence of a particular lengths scales over which size distribution would decay exponentially and resemble the size distribution that one encounters in percolation at the critical point, the percolation threshold.

When analyzing the blood flow characteristics in emerging tumor vasculature of our model we found an interesting phenomenon which is naturally absent in models with a regular starting configuration: Thick arterioles and venoules provide a well conducting support structure around the tumor. Since the total pressure difference between the tree roots is fixed, the transported blood volume is given by the total flow resistance of entire vascular tree. Dilation of a few selected vessels forming a path between the tree roots can remove a bottlenecks formed by thinner vessels. Angiogenesis which provides additional vessels thereby facilitates the creation arterio-venous short-cuts, or shunts, through multiple partly disjoint paths. This leads to an increased blood flow through the tumor vasculature when compared with the starting vasculature. In contrast to this in a regular network the total flow resistance is dominated by the network outside of the tumor (Bartha and Rieger, 2006, Welter et al. 2007) and the flow cannot not increase via the dilation of tumor internal vessels. There are experimental studies which agree with the predictions of our model. In (Sahani et al., 2005) perfusion parameters in rectal cancer were measured via computer tomography where consistently increased blood flow is reported by approximately a factor of two compared to normal tissue. There it is also argue that angiogenesis facilitates the creation of arterio-venous shunts which bypass the capillary network - the same mechanism by which blood increases in our model.

These arterio-venous shunts should also lead to an increased blood pressure range in tumor vasculatures: They connect vessels with high pressure to vessels with low pressure, which then varies continuously within the connecting vessel. Indeed we find a wide spread among pressures over a short range of radii near r_{max} in our model, which is somewhat in contrast with the prevailing view that the pressure as function of vessel radius is reduced in the venous part in tumors (Jain, 1988). Our result indicate that the measure used to assess the relation of tumor blood flow to normal tissue has critical impact on the results. It has been shown that measuring perfusion as function the spatial location can give rise to elevated flow rates, whereas comparison of flow rates between vessels of a certain radius may show either increased as well as decreased flow rates depending on the radius and the location in the vascular hierarchy.

Our drug flow computations again showed that a drug bolus, which is injected into the source arteries of the blood vessel network in our model for some time, reaches all perfused blood vessels, although the thin capillaries in the highly vascularized tumor boundary needs a longer time to become filled with drug. Blood-borne delivery of therapeutics into the tumor-vasculature does not appear to be an obstacle for a successful chemotherapy. The reasons for failure of drug delivery to tumor cells are more likely related to drug uptake the drug transport through the tumor tissue (Minchinton and Tannock, 2006). Since blood is in contact with the interstitial fluid, due to leaks in tumor vessels, fluid exchange can take place with the ECM. This has been shown to lead to steady states with elevated IFP levels, where the difference between micro-vascular pressure (MPD) and IFP generally lower than normal (Boucher et al., 1996). Since convective transport is driven by pressure differences, high IFP could pose a barrier to drug delivery (Hassid et al., 2006)). On

the other hand, leakiness and MVP-IFP gradients could lead to premature release predominantly in locally restricted regions around vessels where blood enters the tumor. Vessels in the outflow regions would thus be depleted of drug. Locally released drug would then be transported by IFP gradients out of the tumor. Furthermore drugs usually consist of large macromolecules. Their low diffusibility through the vessel wall and generally lower diffusibility than O_2 could lead to situations where sufficient O_2 reaches certain TCs to let them remain viable, but not enough drug reaches them to kill them off due to the lower diffusion radius.

In future work it would be useful to study the remodeling of a three dimensional arterio-venous network. Getting access to a realistic initial network is likely to pose a hard problem. In particular if it must be artificially created. Otherwise the extension to 3d is straight forward and has already been done in (Lee et al., 2006) with similar results. Further aspects to assess are interstitial fluid transport and O_2 release with associated intra-vascular O_2 decrease. Furthermore implementation of a tumor model which supports quantitative assessment of stresses in the tissue appears mandatory for studies of irregular tumor morphologies.

References

Bartha, K., Rieger, H., 2006. Vascular network remodeling via vessel cooption, regression and growth in tumors. *J. Theor. Biol.* 241, 903-918.

Baish, J. W., Jain, R. K., 2000. Fractals and Cancer. *Persp. Cancer Res.* 60, 3683–3688.

Belien, J.A., Somi, S., de Jong, J.S., van Diest, P.J., Baak, J.P., 1999. Fully automated microvessel counting and hot spot selection by image processing of whole tumor sections in invasive breast cancer. *J. Clin. Path.* 52, 184-192.

Carmeliet, P., Jain, R. K., 2000. Angiogenesis in cancer and other diseases. *Nature*, 407, 249-257.

Carmeliet, P., Tessier-Lavigne, M., 2005. Common mechanisms of nerve and blood vessel wiring. *Nature* 436, 193-200.

Cassot, F., F. Lauwers, C. F., Prohaska, S., Lauwers-Cances, V., 2006. A Novel Three-Dimensional Computer-Assisted Method for a Quantitative Study of Microvascular Networks of the Human Cerebral Cortex. *Microcirculation* 13, 1-18.

Chung, H.-W., Chung, H.-J., 2001. Correspondence re: J. W. Baish and R. K. Jain, *Fractals and Cancer*. *Cancer Res.*, 60: 3683-3688. *Cancer Res.* 61, 8347–8351.

Döme, B., Paku, S., Somlai, B., Tímár, J., 2002. Vascularization of cutaneous melanoma involves vessel co-option and has clinical significance. *J. Path.* 197, 355-362.

Erber, R., Eichelsbacher, U., Powajbo, V., Korn, T., Djonov, V., Lin, J., Hammes, H.-P., Grobholz, R., Ullrich, A. Vajkoczy, P., 2006. EphB4 controls blood vascular morphogenesis during postnatal angiogenesis. *EMBO* 25, 628-641.

Folkman, J., Bach, M., Rowe, J.W., Davidoff, F., Lambert, P., Hirsch, C., Goldberg, A., Hiatt, H.H., Glass, J., Henshaw, E., 1971. Tumor angiogenesis therapeutic implications. *N. Engl. J. Med.* 285, 1182-1186.

Folkman J., 1990. What is the evidence that tumors are angiogenesis dependent. *J. Natl. Cancer Instit.* 82, 4-6.

Gödde, R., Kurz, H., 2001. Structural and Biophysical Simulation of Angiogenesis and Vascular Remodeling. *Dev. Dyn.* 220, 387-401.

Hassid, Y., Furman-Haran, E., Margalit, R., Eilam, R., Degani, H., 2006. Noninvasive Magnetic Resonance Imaging of Transport and Interstitial Fluid Pressure in Ectopic Human Lung Tumors. *Cancer Res.* 66, 4159-4166.

Hannahan, D., Folkman J., 1996. Patterns and emerging mechanisms of the angiogenic switch during tumorigenesis. *Cell* 86, 353-364.

Höckel, S., Schlenger, K., Vaupel, P., Höckel, M., 2001. Association between host tissue vascularity and the prognostically relevant tumor vascularity in human cervical cancer. In. *J. Oncol.* 19, 827-832.

Holash, J., Maisonpierre, P. C., Compton, D., Boland, P., Alexander, C. R., Zagzag, D., Yancopoulos, G. D., Wiegand, S. J., 1999a. Vessel Cooption, Regression, and Growth in Tumors

Mediated by Angiopoietins and VEGF. *Science* 284, 1994-1998.

Holash, J., Wiegand, S., Yancopoulos, G., 1999b. New model of tumor angiogenesis: dynamic balance between vessel regression and growth mediated by angiopoietins and VEGF. *Oncogene* 18, 5356-5362.

Kullander, K., Klein, R., 2002. Mechanisms and functions of Eph and ephrin signalling. *Nature Rev. Mol. Cell. Biol.* 3, 475-486.

Mandelbrot, B.B., 1982. *The fractal geometry of nature*. Freeman, New York.

McDonald, D. M., Choyke, P. L., 2003. Imaging of angiogenesis: from microscope to clinic. *Nature Med.* 9, 713-725.

Minchinton, A. I., Tannock, I. F., 2006. Drug penetration in solid tumours. *Nature Reviews Cancer* 6, 583-592.

Mironov, V., Little, C., Sage, H. (Eds.), 1998. *Vascular Morphogenesis: in Vivo, in Vitro, in Mente*. Birkhäuser Boston.

Murray, C. D., 1926. The physiological principle of minimum work: The vascular system and the cost of blood volume. In: *Proc. Natl. Acad. Sci. USA*, vol. 12, 207-214.

Pahernik, S., Griebel, J., Botzlar, A., Gneiting, T., Brandl, M., Dellian, M., Goetz, A. E., 2001. Quantitative imaging of tumour blood flow by contrast-enhanced magnetic resonance imaging. *Brit. J. Canc.* 85, 1655-1663.

Paku, S., 1998. Current concepts of tumor-induced angiogenesis. *Pathol. Oncol. Res.* 4, 62-75.

Pries, A. R., Reglin, B., Secomb, T. W., 2005. Remodeling of Blood Vessels: Responses of Diameter and Wall Thickness to Hemodynamic and Metabolic Stimuli. *Hypertension* 46, 725-731.

Pries, A. R., Secomb, T. W., Gaehtgens, P., 1995. Design principles of vascular beds. *Circ. Res.* 77, 1017-1022.

Schreiner, W., Buxbaum, P.F., 1993. Computer-optimization of vascular trees. *IEEE Trans. Biomed. Eng.* 40, 482-491.

Welter, M., Rieger, H., Bartha, K., 2007. Emergent vascular network inhomogeneities and resulting blood flow patterns in a growing tumor. To be published in *J. Theor. Biol.*

Weidner, N., 1995. Current pathological methods for measuring intratumoral microvessel density within breast carcinoma and other solid tumors. *Breast Canc. Res. Treat.* 36, 169-180.

Tables

Table 1: Listing of model parameters with values for our base case simulation runs.

Parameter	Value	Description	Reference
$\delta^{(gen)}$	60 μm	Lattice const. (Tree-generator)	
δ	10 μm	Lattice const. (Tumor-model)	
L	1200	Lattice size (Tumor-model)	
Δt	1 h	Time step	
$ T(t = 0) $	1000	Initial number of TCs	
$\alpha^{(0)}$	0.02	O ₂ source coefficient	(Secomb et al. 2004)
$\kappa^{(Nmm)}$	$(80 \mu\text{m})^{-2}$	consumption in normal tissue	(Carmeliet and Jain, 2000)
$\kappa^{(T)}$	$4\kappa^{(Nmm)}$	consumption tumor tissue	
$\theta_o^{(prol)}$	$0.3 \approx 0.9\langle c_o \rangle$	TC O ₂ prol. threshold	
$c_o^{(B)}$	0.45	dimensionless blood-O ₂ level	
$\theta_o^{(death)}$	$\theta_o^{(prol)}/10$	TC hypoxia threshold	
$R^{(g)}$	200 μm	Growthfactor diffusion radius	(Nehls et al. 1998)
$\theta_g^{(prol)}$	10^{-4}	sprouting GF threshold	
$t_{TC}^{(uo)}$	100 h	TC survival time under hypoxia	(Yu et al. 2002)
$t_{TC}^{(prol)}$	10 h	TC proliferation time	
$t_{EC}^{(sprout)}$	5 h	Sprout initiation/extension time	
$t_{EC}^{(dil)}$	40 h	Vessel dilation time	(Döme et al. 2002)
$s^{(max)}$	100 h	Time till sprout regression	(Nehls et al. 1998)
$t_{EC}^{(switch)}$	25 h	Time till switch to circumferential growth	
Δw	0.04 $\mu\text{m}/\text{h}$	Wall thickness/stability decrease rate	
$r^{(init)}$	4 μm	Initial vessel radius	
$r^{(max)}$	25 μm	Max. vessel radius	(Döme et al. 2002)
$l^{(spr)}$	20 μm	Min. distance between junctions	(Döme et al. 2002)
$f^{(c,max)}$	1 Pa	Peak critical shear force	
$p^{(c,max)}$	0.1	Peak collapse probability	

Figure captions

Fig.1: Illustration of the model state: All discrete elements are aligned at the triangular lattice shown in the background. Blue bars represent vessels occupying bonds. The set containing all vessels is denoted by V . One vessel is highlighted by a black frame, its junctions to other vessels are denoted by $\mathbf{x}_1, \mathbf{x}_2$. Tumor cells (TCs) can occupy lattice sites with a one to one relationship. The set containing TCs is denoted as T . One TC is displayed as yellow hexagon.

Fig.2: Sketch of the dynamical processes in the model: (a) TC Proliferation, (b) TC Death, (c) Sprout formation, (d) Sprout migration, (e) Vessel regression and removal, (f) Dilation and wall degradation. See text for details.

Fig.3: Examples of starting configurations of the model at $t = 0$ h. We chose four different basic layouts for the vascular network denoted as A,B,C,D. They differ in the placement and lengths of major supply-and drain vessels, which are randomly distributed. This is indicated in the top right inlets. Arteries are red, veins blue, black bars show intervals from which starting locations are drawn while the wedge shaped part of the red/blue bars indicate intervals from which starting lengths are drawn. The color code of the resulting networks shows the blood pressure distribution from 2kPa (red) to 12kPa (blue). The small yellow area in the system center is the tumor nucleus initialized by eden growth to maximum of 1000 TCs. The background in normal tissue/extracellular matrix is colored green if the growthfactor is sufficient to enable sprouting. Otherwise those areas are white.

Fig.4: Snapshots of the dynamical evolution at times $t = 0, 200, 600$ h of the model in a single simulation run starting in configuration A (shown in Fig. 3a) at $t = 0$. Viable TCs are bright yellow, while necrotic regions are dark yellow. Vessels are color coded by blood pressure as in Fig.3. The background in normal tissue/extracellular matrix is colored green if the growthfactor is sufficient to enable sprouting. Otherwise those areas are white.

Fig.5: Final configuration at $t = 1200$ h for the simulation run depicted in Fig.4. The color code is identical to Fig.4. Note how vessels in the tumor center serve as arteriovenous shunts. They have dilated diameters and thus carry high blood throughput. The formation of hot spots with increased local MVD is also evident.

Fig.6: Final configurations at ($t = 1200$ h) of simulation runs of the model starting with the initial configurations B, C, D shown in Fig.3. The color code is identical to Fig.4. The formation of hot spots is clearly visible in the central region in B, but not so in C and D. There increased MVD can be observed in a few locations close to the tumor boundary.

Fig.7: Magnified view of the tumor boundary showing in detail how the vasculature is remodeled close to the invasive edge. Alternating with very high MVD on small scale, there are “holes” of the size of the intervascular distance in normal tissue. This is an effect of prohibiting sprouts from arteries, which would otherwise fill the holes, leading to a homogeneous vascular density. Behind the peripheral zone, the MVD drops rapidly. One can further see a few isolated dilated vessels directly connected to arterioles/venoules in healthy tissue beyond the invasive edge. For the color code see the caption of Fig.4.

Fig.8: Flow rate distribution in the tumor vessel network depicted in Fig.5. The color code is on a logarithmic scale as indicated on the left side. The flow rate here is the blood volume per time through the vessel cross-section, closely related to the blood flow per tissue volume as commonly measured in experiments. Dilated tumor-internal vessels usually exhibit high flow rates. If one would measure in/outflow per tissue volume element as in dynamic MRT (magnetic resonance tomography) measurements (Pahernik et al., 2001) one would observe hot-spots located at the respective high-MVD zones.

Fig.9: Radial distributions of various quantities characterizing the dynamical development of the compartmentalization of the tumor vasculature in the model: The radius r here denotes the distance from the tumor center. One data point represents an average over a concentric $50\mu\text{m}$ wide shell, and over 40 simulation runs, 10 per configuration A,B,C,D (see text or Fig.3). (a) shows the micro vascular density, (b) the O_2 level and (c) the tumor cell density. The right column shows blood flow related variables: (d) the vessel radius, (e) the flow rate and (f) the shear force, which are in contrast to (a),(b),(c) given as the average over actually occupied sites within a shell, instead of over all sites. For $t=1200\text{h}$ also the local variations (root mean square deviations) are indicated as error bars.

Fig.10: Scatter plots showing hydrodynamic quantities for individual vessel segments as a function of the vessel radius: (a) blood pressure, (b) wall shear force, and (c) flow rate through the vessel cross section. Each data point is a sample from a randomly chosen position, uniformly distributed over the vascular network. Samples from both, the initial vasculature at $t=0\text{h}$, and the tumor network at $t=1000\text{h}$ are shown. For the former, arteries are displayed in red with negative radius, veins are blue and capillaries are pink. Tumor vessels that were initially arteries are displayed yellow, those that were veins are light blue. New vessels and capillaries are black. Dilation causes the latter vessels to span radius values from 5 to $25\mu\text{m}$ (the maximum dilation radius $r^{(max)}$), but due to the lack of hierarchical organization in the tumor they cannot contribute to arteries or veins. Therefore respective data points were put with probability 1/2 on one or the other side. Note that tumor vessels capped at $r^{(max)}$ display a much larger range of values than normal (see text). Also note that (b) and (c) are presented as linear-log plots.

Fig.11: Final configuration at $t=1200\text{h}$ of a simulation run using an alternate vessel collapse rule where vessel collapses are restricted to a thin band (here $400\mu\text{m}$ in width) behind the invasive edge. The collapse probability $p_{ring}^{(c)}$ is thus modulated with an appropriate term which depends on the distance to the tumor center (see text). In this instance, parameters are such that the mean survival time of instable vessels is of the order of the time they spend in the “collapse region”, leading to a dominant role of the random collapse process for the resulting morphologies, and putting the system near a transition to a fully vascularized tumor. The parameter set is the same as in the base case, except for the critical shear force $f^{(c,max)}$ which is set to 3Pa, instead of 1Pa.

Fig.12: Local MVD in the tumor vasculature versus local pressure gradient $\langle|\Delta P|\rangle$ (i.e. blood pressure differences between neighboring vessels) in the starting vasculature. In the main plot data points are averaged over different runs of the base case scenario, the averages are taken over the entire tumor interiors (excluding the vascularized boundary region) at $t=1200\text{h}$. The inset is a scatter plot for a single simulation run, where the average is performed locally over a small disc with radius $150\mu\text{m}$ (see Fig.13).

Fig.13: Digitized data processing of network configurations demonstrating the correlation between the intervascular pressure gradient in the starting network with the local MVD in the tumor network. (a) Local magnitude of the “intervascular pressure” gradient $\|\Delta P\|$ in the initial network (see text). (b) Smoothing of the data in a: locally averaged values of $\|\Delta P\|$ were computed at randomly distributed locations, each by averaging over a $150\mu\text{m}$ -radius disc, then the space closest to some data point is filled with a gray scale value proportional to $\langle\|\Delta P\|\rangle$. (c) Local MVD of the tumor network. (d) Smoothing of the data in c, analogous to b, yielding an estimate for locally averaged MVD. Value ranges are 0-45 (black to white) for $\|\Delta P\|$ and 0-0.4 for the MVD. Note that in d the local MVD is highest (brightest) in regions in the upper half of the network, and in b the local pressure gradient is highest (brightest) also in regions in the upper half of the network.

Fig.14: Shows probability distributions in log-log plots, for (a) the local MVD, given as the local average over $250\mu\text{m}$ wide boxes, (b) the volume of necrotic tissue clusters, defined as the number of sites in respective connected components of dead tissue. (c) the volume of vessel

hot-spot areas, defined as the connected components of regions where the local MVD exceeds a threshold (0.15). The distributions are generated by binning observed values in histograms over 40 simulation runs (at $t=1200h$). Note that the distributions show algebraic decay. In this instance in particular with the same exponent within the error bounds which are of the order of 2%.

Fig.15: Snapshots of the drug-flow simulation using the configuration A tumor at $t=1000h$. The color code shows the drug concentration as indicated on the scale bar. Note that drug reaches most parts of the vasculature quickly in a few seconds at the maximum concentration. In the $T=6.6s$ snapshots a few vessels in the boundary region are not yet perfused. The time until drug saturates the complete vasculature is of the order of minutes. We can observe this behavior generally for all resulting networks.

Fig.16: (a) shows the amount of vessels given as the fraction of total tumor network length that has been exposed to a drug concentration larger than the indicated concentration c_{max} (at $t=20s$ of the drug simulation). The black line represents the average over 40 runs with different networks. (b) shows the amount of vessels given as the fraction of total tumor network length that has been exposed to a drug concentration larger than 0.25 for longer than indicated time t_e . The black line represents the average over 40 runs with different networks. Like in Fig.15, tumor networks from the base case at $t=1000h$ where used.

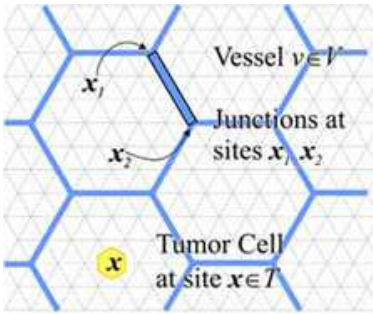


Fig. 1

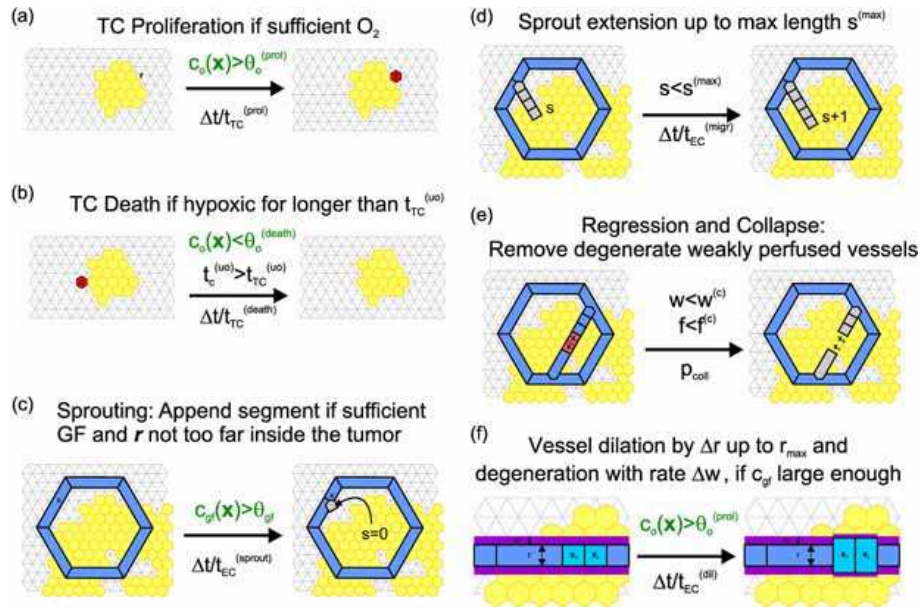


Fig. 2

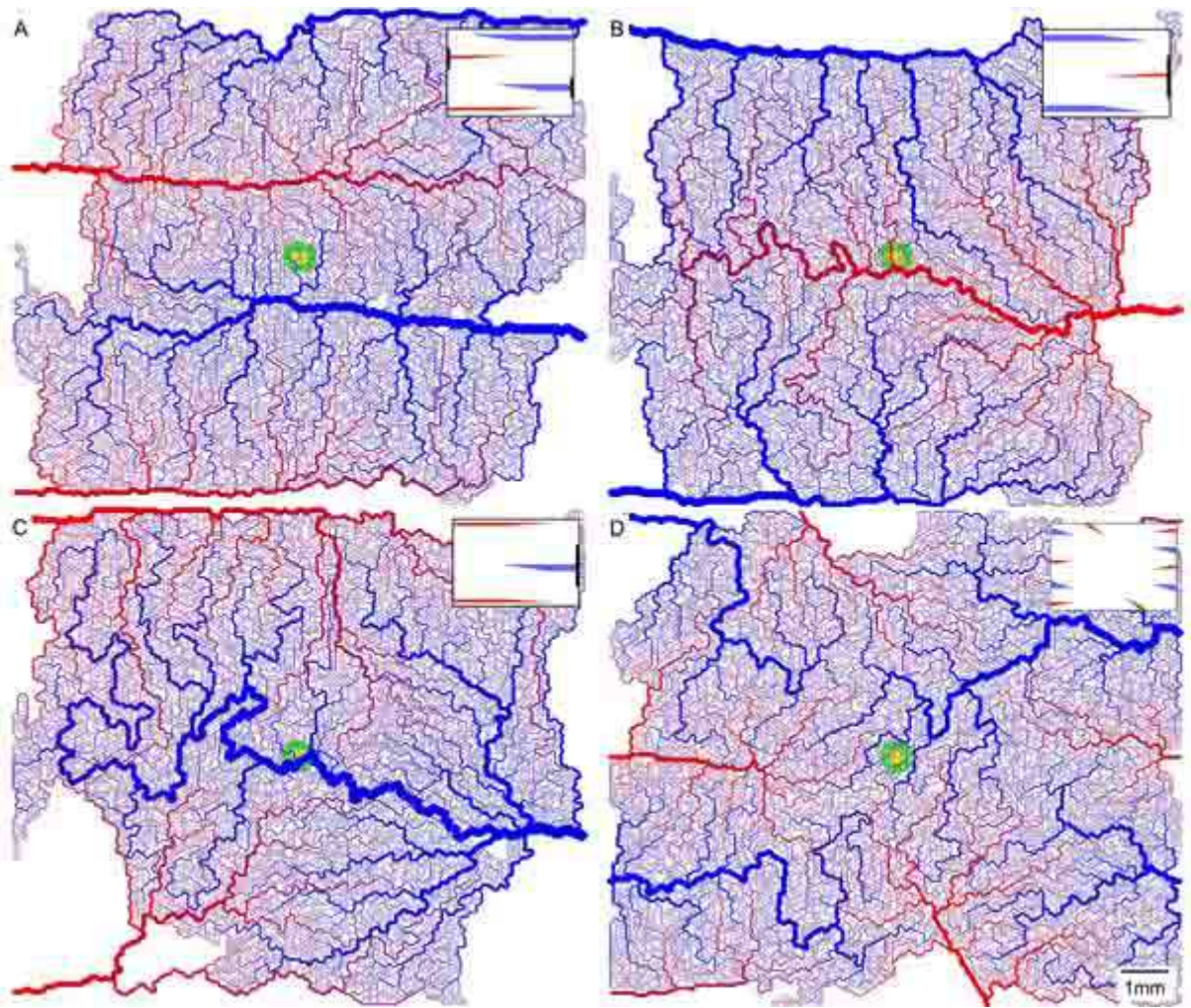


Fig. 3

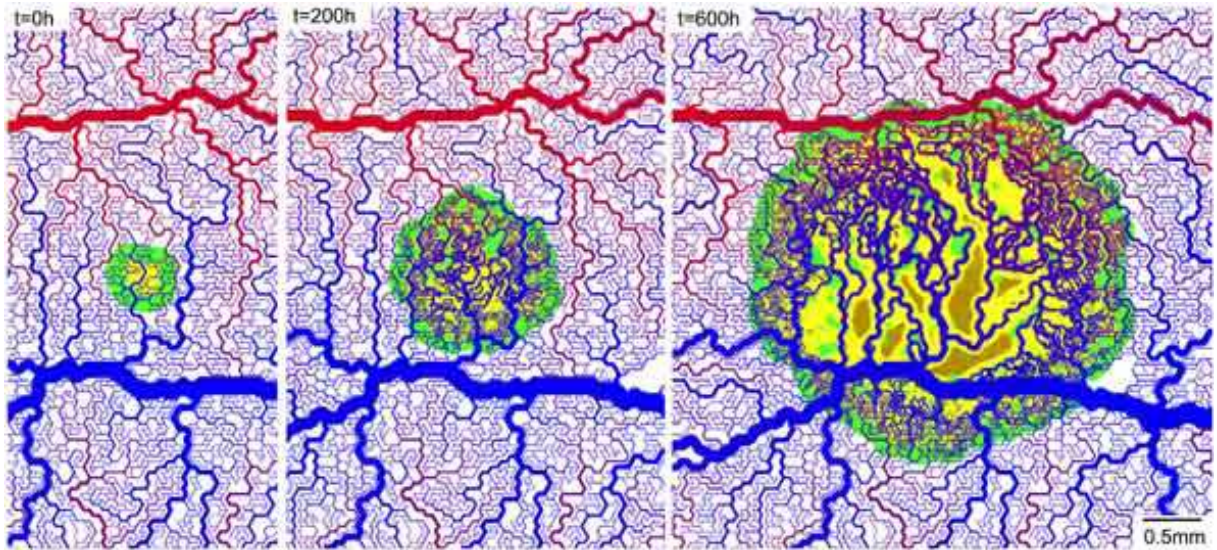


Fig. 4

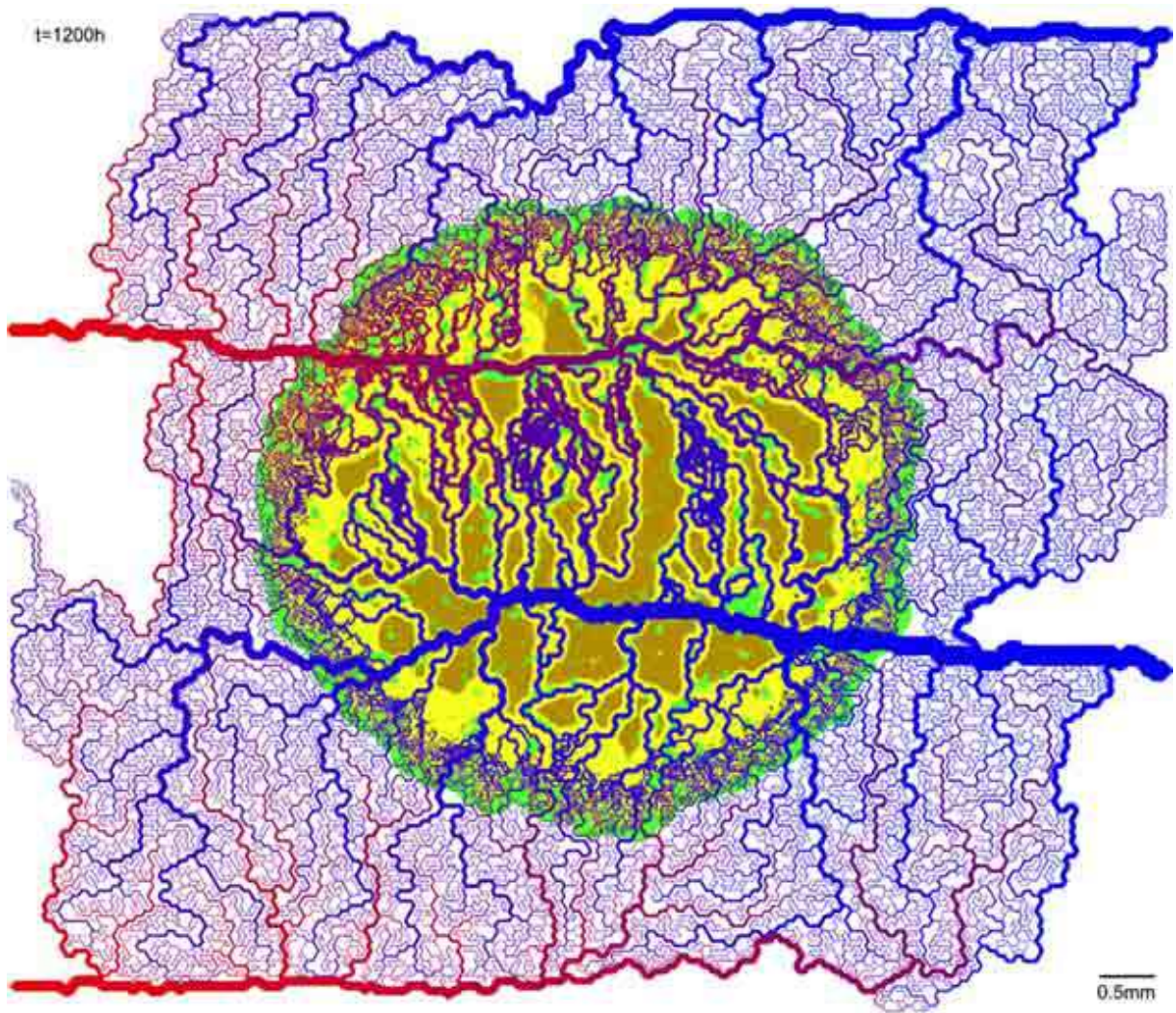


Fig. 5

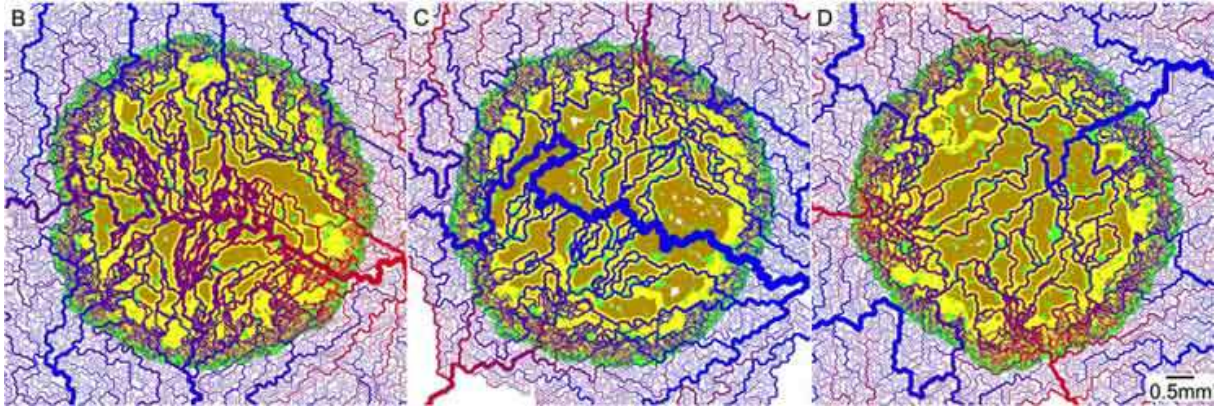


Fig. 6

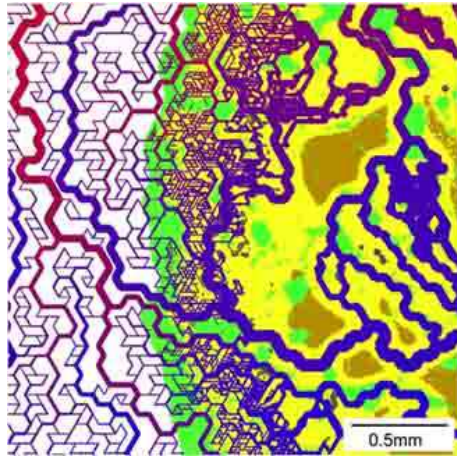


Fig. 7

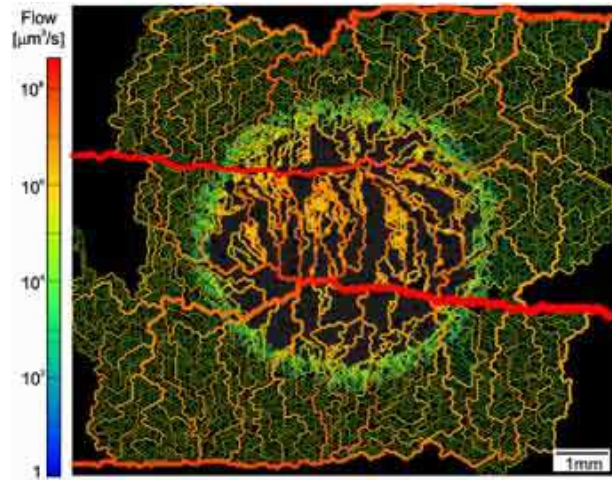


Fig. 8

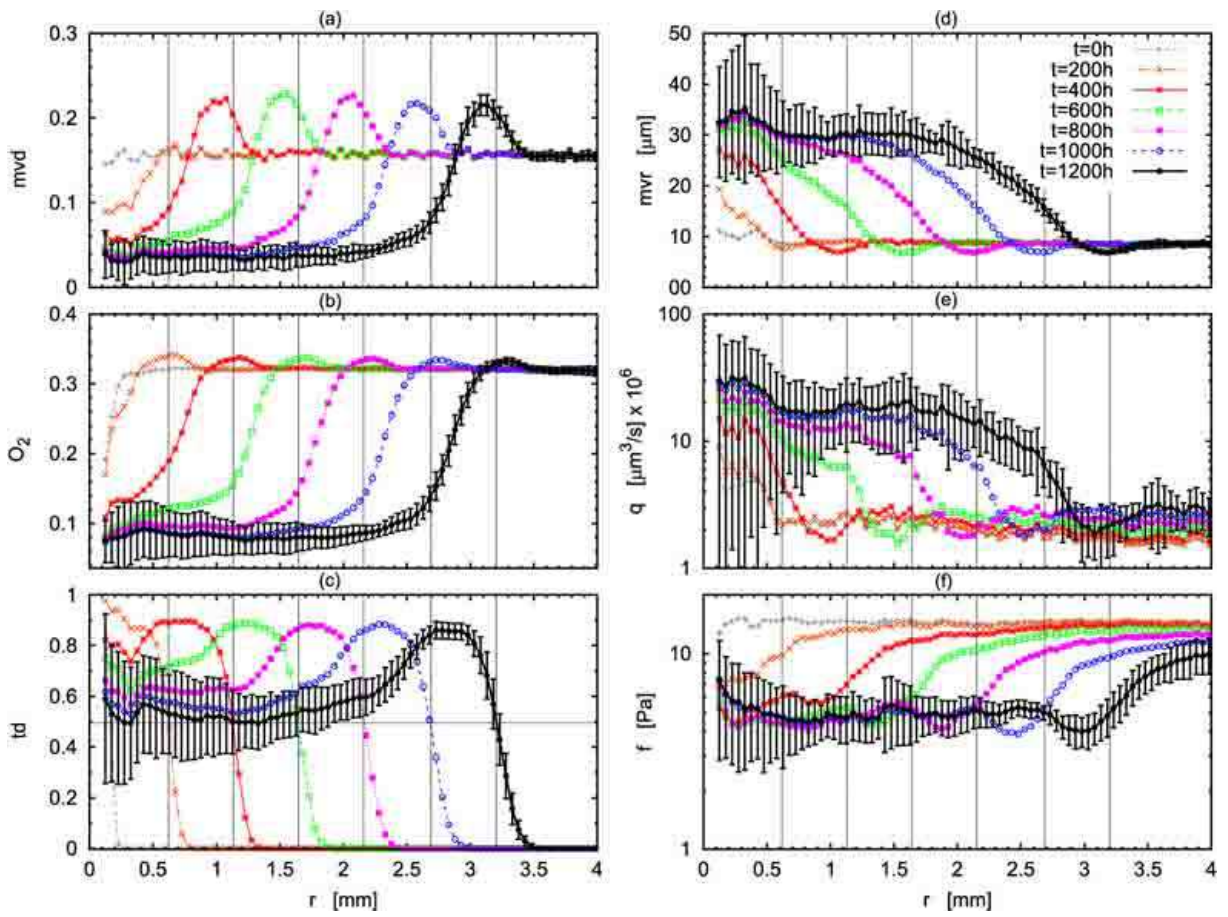


Fig. 9

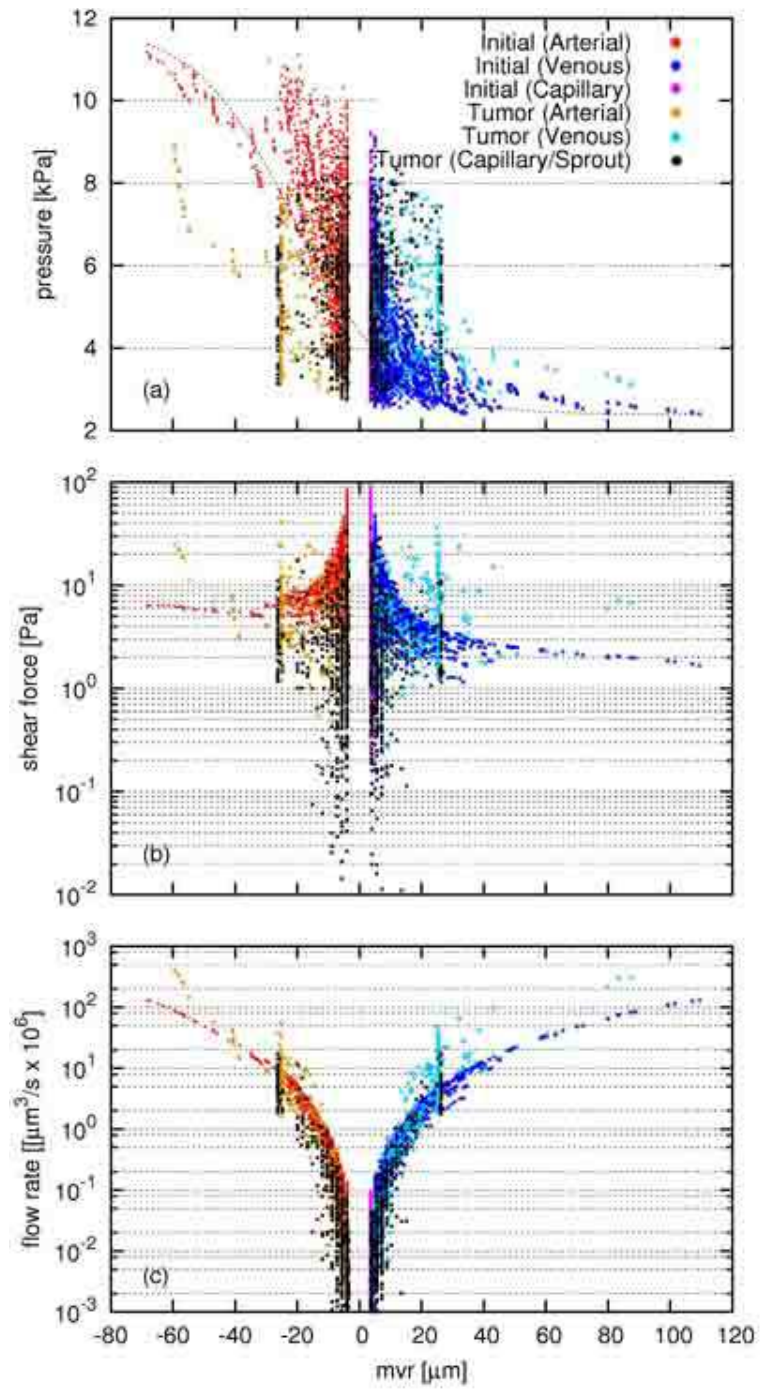


Fig. 10

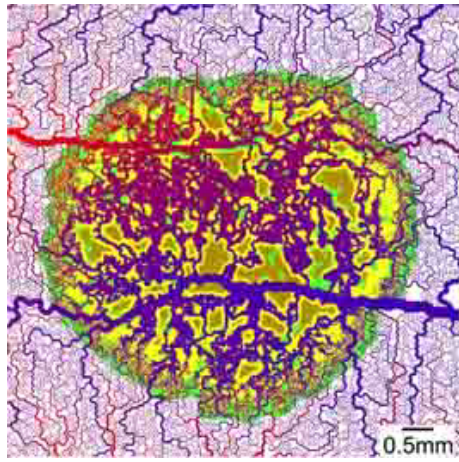


Fig. 11

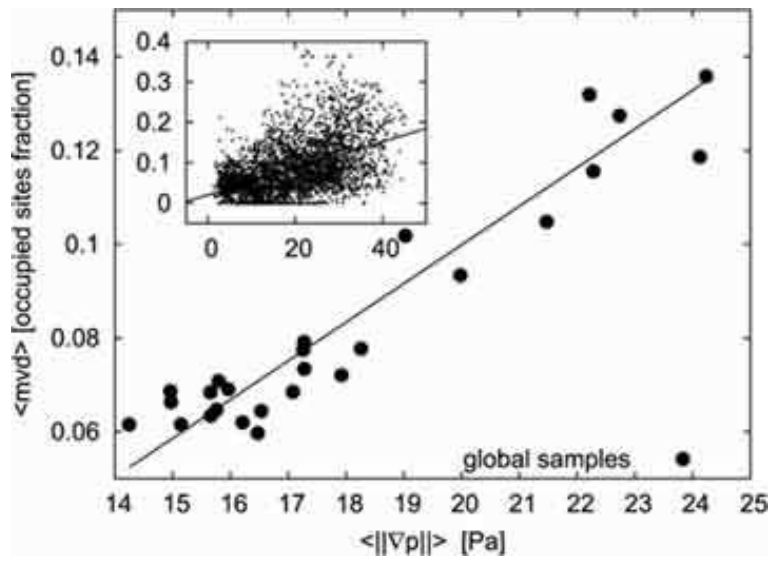


Fig. 12

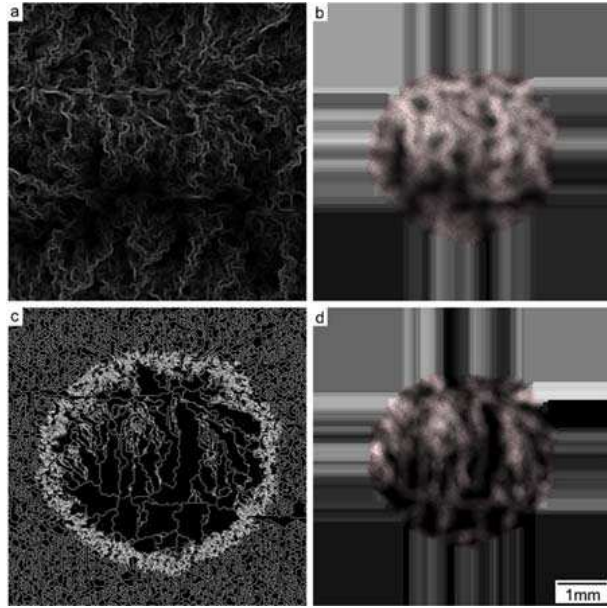


Fig. 13

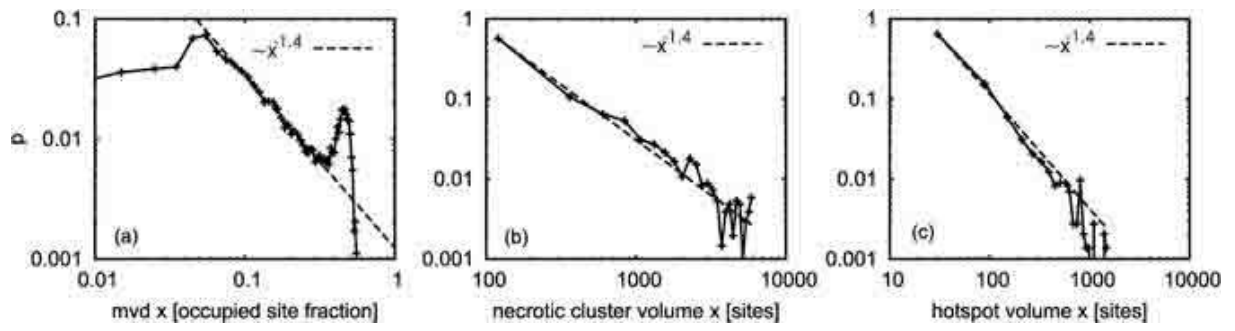


Fig. 14

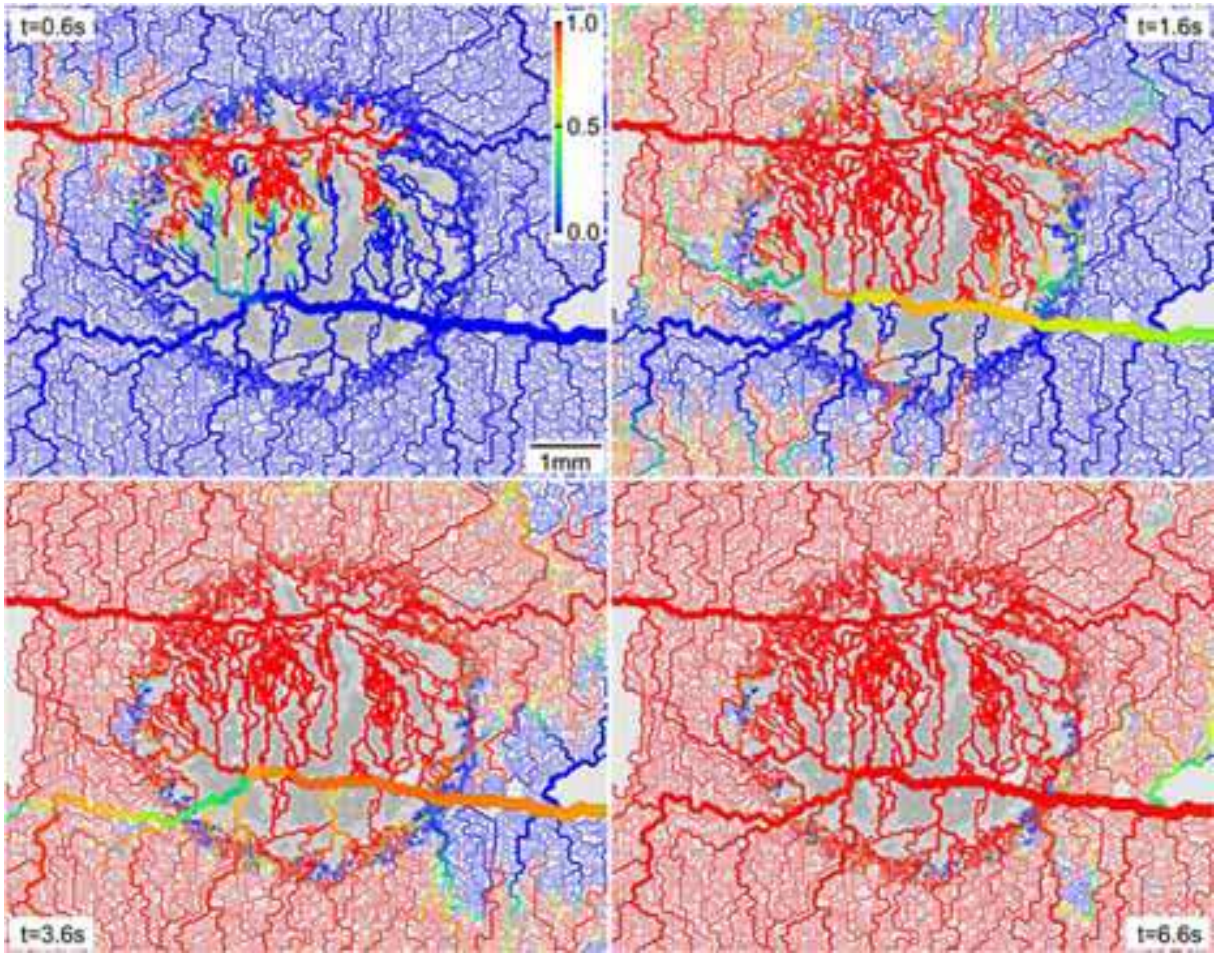


Fig. 15

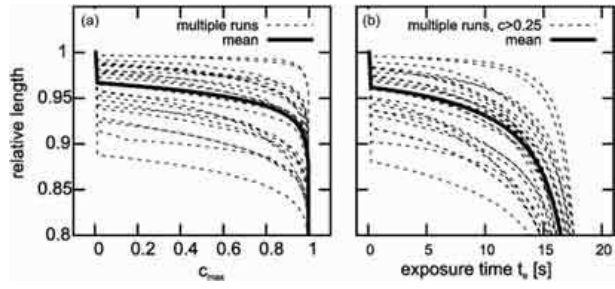


Fig. 16